

Article

Synthesis of Polyaniline Supported CdS/CdS-ZnS/CdS-TiO₂ Nanocomposite for Efficient Photocatalytic Applications

Nida Qutub ^{1,*}, Preeti Singh ², Suhail Sabir ³, Khalid Umar ⁴ , Suresh Sagadevan ^{5,*} and Won-Chun Oh ^{6,*} ¹ Department of Chemistry, Jamia Millia Islamia, New Delhi 110025, India² Department of Fibers and Textile Processing Technology, Institute of Chemical Technology, Mumbai 400019, India; aries.pre84@gmail.com³ Department of Chemistry, Aligarh Muslim University, Aligarh 202002, India; drsuhailsabir@gmail.com⁴ School of Chemical Sciences, Universiti Sains Malaysia (USM), Penang 11800, Malaysia; khalidumar4@gmail.com⁵ Nanotechnology & Catalysis Research Centre, University of Malaya, Kuala Lumpur 50603, Malaysia⁶ Department of Advanced Materials Science and Engineering, Hanseo University, Seosan-si 356-706, Chungnam, Korea

* Correspondence: dmidaqutub@gmail.com (N.Q.); drsureshnano@gmail.com (S.S.); wc_oh@hanseo.ac.kr (W.-C.O.)

Abstract: Photocatalytic degradation can be increased by improving photo-generated electrons and broadening the region of light absorption through conductive polymers. In that view, we have synthesized Polyaniline (PANI) with CdS, CdS-ZnS, and CdS-TiO₂ nanocomposites using the chemical precipitation method, characterized and verified for the photo-degradation of Acid blue-29 dye. This paper provides a methodical conception about in what way conductive polymers “PANI” enhances the performance rate of composite photocatalysts (CdS, CdS-ZnS and CdS-TiO₂). The nanocomposites charge transfer, molar ratio, surface morphology, particle size, diffraction pattern, thermal stability, optical and recombination of photo-generated charge carrier properties were determined. The production of nanocomposites and their efficient photocatalytic capabilities were observed. The mechanism of photocatalysis involved with PC, CZP and CTP nanocomposites are well presented by suitable diagrams representing the exchange of electrons and protons among themselves with supported equations. We discovered that increasing the number of nanocomposites in the membranes boosted both photocatalytic activity and degradation rate. CdS-Zinc-PANI (CZP) and CdS-TiO₂-PANI(CTP) nanocomposites show entrapment at the surface defects of Zinc and TiO₂ nanoparticles due to the demolition of unfavorable electron kinetics, and by reducing the charge recombination, greater photocatalytic activity than CdS-PANI (CP) with the same nanoparticle loading was achieved. With repeated use, the photocatalysts’ efficiency dropped very little, hinting that they may be used to remove organic pollutants from water. The photocatalytic activity of CZP and CTP photocatalytic membranes was greater when compared to CdS-PANI, which may be due to the good compatibility between CdS and Zinc and TiO₂, as well efficient charge carrier separation. PANI can also increase the split-up of photo-excited charge carriers and extend the absorption zone when combined with these nanoparticles. As a result, the development of outrageous performance photocatalysts and their potential uses in ecological purification and solar power conversion has been facilitated. The novelty of this article is to present the degradation of AB-29 Dye using nanocomposites with polymers and study the enhanced degradation rate. Few studies have been carried out on polymer nanocomposites and their application in the degradation of AB-29 dyes and remediation of water purposes. Nanoparticle CdS is a very effective photocatalyst, commonly used for water purification along with nanoparticle ZnS and TiO₂; but cadmium ion-leaching makes it ineffective for practical and commercial use. In the present work, we have reduced the leaching of hazardous cadmium ions by trapping them in a polyaniline matrix, hence making it suitable for commercial use. We have embedded ZnS and TiO₂ along with CdS in a polyaniline matrix and compared their photocatalytic activity, stability, and reusability, proving our nano-composites suitable for commercial purposes with enhanced activities and stabilities, which is a novelty. All synthesized nanocomposites



Citation: Qutub, N.; Singh, P.; Sabir, S.; Umar, K.; Sagadevan, S.; Oh, W.-C. Synthesis of Polyaniline Supported CdS/CdS-ZnS/CdS-TiO₂ Nanocomposite for Efficient Photocatalytic Applications. *Nanomaterials* **2022**, *12*, 1355. <https://doi.org/10.3390/nano12081355>

Academic Editor: Vasco Teixeira

Received: 9 March 2022

Accepted: 12 April 2022

Published: 14 April 2022

Publisher’s Note: MDPI stays neutral with regard to jurisdictional claims in published maps and institutional affiliations.



Copyright: © 2022 by the authors. Licensee MDPI, Basel, Switzerland. This article is an open access article distributed under the terms and conditions of the Creative Commons Attribution (CC BY) license (<https://creativecommons.org/licenses/by/4.0/>).

are active within the near-ultraviolet to deep infrared (i.e., 340–850 nm). This gives us full efficiency of the photocatalysts in the sunlight and further proves the commercial utility of our nanocomposites.

Keywords: nanoparticles; conducting polymer; Acid blue-29 dye; photocatalytic mechanism

1. Introduction

Sludge, urban run-off, agriculture wastewater, industrial wastewater treatment plants, food processing, pulp and paper manufacturing, and aquaculture all contribute to organic pollution. Pesticides, fertilizer, solvents, phenolic compounds, plasticizers, polycyclic aromatic hydrocarbons, cleansers, lubricants, heavy oils, pharmaceuticals, enzymes, and polysaccharides are examples of organic pollutants that are extremely toxic to both the environment and living things. Among all these organic pollutants, organic dyes are considered the chief hazardous pollutant to the environment and living things because they can block sunlight from entering the water stream, limiting photosynthetic reactions, and some forms of organic dyes are extremely poisonous and even cancer-causing. These dyes are increasingly employed in the leather, plating, fiber and textile, papermaking, plastics, and lithography sectors [1]. Furthermore, they color the wastewater, causing aesthetic concerns. Dyes have a complex aromatic structure that makes them more stable and difficult to remove from effluents [2]. However, if dyestuffs-containing effluents are not properly treated, they can pose serious environmental problems. As a result, the removal of organic dyes is critical for alleviating the water difficulties that the environment and humans confront [3–5]. Acid dye 29, an anionic dye, is commonly used in the fiber and textile industry for dyeing all-natural fibers, silk and synthetics, which are utilized to a lesser extent in several applications such as paints, plastics, and leather. However, due to the lack of confirming animal or human evidence, Acid dye has not been categorized as “toxic by consumption”. However, following intake, it may harm an individual’s health, particularly if they have pre-existing organ damage (e.g., liver, kidney), gastrointestinal tract pain, redness in the eyes, or skin irritation concerns [6].

Chemical, biological, and physical treatment methods for eliminating contaminants from wastewater have been developed and are now widely used [7]. Adsorption is one of these approaches that has received a lot of attention due to its small cost and great efficiency, as well as its ease of use [8–16]. As an adsorbent, organic and inorganic composite materials can promote synergistic adsorption and broaden the application [17,18]. Previous research has shown that both photocatalytic degradation and photocatalytic hydrogen production can be carried out with semiconductor photocatalysts, which can overcome many issues. If pollution oxidation and oxygen reduction do not occur concurrently, the extent of electron and hole recombination increases due to an upsurge in electrons in the conduction band. As a result, preventing electron build-up is critical for efficient photocatalytic oxidation. These redox processes have formed the necessary part of the photocatalytic mechanism [19]. These semiconductors have been shown to use UV light, accounting for just 3–5% of the solar range, which is responsible for their drawback and commercial applicability [20]. The photocatalytic activity could be improved with the manipulation of the semiconductor’s bandgap [21], which extends the light absorption of semiconductor materials to visible areas. As a result, there has been a surge in interest in the development of semiconductor materials that emit visible light. The numerous strategies for developing visible light-responsive semiconductor materials include noble metals doping, non-metallic doping, and metal/non-metal co-doping [22–24].

Many in-organic polymers nanocomposites comprising various groupings of two or more components have gained increased consideration in current research due to their intriguing physical properties and prospective uses [25–27]. The polymer governing the nucleation of nanoparticles may cause their growth to be inhibited by embedding or encapsulating them in the polymer [28]. It also helps with the film’s casting and particle

dimension dispersal. Due to the fast separation of charges by inducing the light and considerably delayed recombination of charges, materials with delocalized conjugated structures have been extensively studied in this field [29]. The use of conductive polymers (such as polythiophene, polyaniline, and polypyrrole) to improve the performance of composite photocatalysts for photocatalytic hydrogen production, antibacterial, and photocatalytic destruction of dangerous substances is reviewed. In composite photocatalysts, conductive polymers can reduce photogenerated electron-hole pair recombination by matching band topologies with other inorganic semiconductors [30]. As a result, conducting polymers with extended-conjugated structures, as well as their derivatives, have attracted a lot of attention as photocatalytic absorbers with the potential to improve semiconductor photo-response. PANI, in particular, is a good photosensitizer that can change TiO₂ photocatalytic properties [31].

Several papers have been published that describe the fabrication of photoactive polyaniline (PANI) nanocomposites with semiconductors such as PANI/TiO₂ [32], PANI/BiVO₄ [33], PANI/SiO₂ [34], PANI/SnO₂ [35], PANI/CdS [36], PANI/V₂O₅ [37] and PANI/Fe₃O₄/SiO₂/TiO₂ [38]. Anion-type pollutants, such as phosphate ions and anionic azo dyes, have also been created and demonstrated to be excellent adsorbents with PANI/TiO₂ composites, and there is a plethora of research based on PANI'S adsorption capability and good stability with semiconductors in terms of dye degradation [39]. However, because polyaniline is a *p*-type semiconductor and CdS nanoparticles are *n*-type, combining the two will result in effective photoconductive and photocatalysis nanocomposites [40]. The semiconductor nanomaterials PbS, ZnS, ZnSe, and CdSe, belonging to the elemental group II-VI, were intensively explored due to their size-dependent optical characteristics [41–44]. Titanium (TiO₂) nanoparticles are intriguing due to their unique physical and chemical properties, which are widely used in the applications of coatings, solar cells, and photocatalysts [45]. Due to their large band gaps, TiO₂ and ZnS are effective photocatalysts; however, it could be activated by UV light, which accounts for solar radiations just about 4–6%; PANI–TiO₂ composites have a narrower bandgap than pure TiO₂ nanoparticles, which allows PANI–TiO₂ to absorb more photons and hence, improved the photocatalytic efficiency of TiO₂ in sunlight [46]. PANI/TiO₂ nanocomposites have exceptional characteristics as they are the donors and acceptors of the electron [47–51]. CdS–TiO₂ and CdS–ZnS sandwich-type nanocomposites were created by combining CdS with TiO₂ and ZnS to boost the photocatalytic activity of CdS, after a few repeating cycles, which could be related to photo-corrosion of CdS. All of the photocatalytic membranes showed a minor decrease in photocatalytic activity when used often [52,53].

In the present study, CdS–ZnS and CdS–TiO₂ were deposited on the PANI substrate to prevent Cd²⁺ ion leaching. PANI was used to examine the effects of CdS, CdS–ZnS, and CdS–TiO₂ nanoparticles on the fundamental properties of the synthesized materials. The outcome of this study will add to our understanding of how to make conducting polymer/semiconductor nanocomposites with desirable nanostructures for use as high-performance photocatalysts in environmental purification and solar energy conversion.

2. Methodology

2.1. Materials

The materials used were Aniline, Chloroform, Sulphuric Acid (H₂SO₄), Ammonium Persulphate (APS), Cadmium Nitrate (Cd(NO₃)₂), Methanol, Zinc chloride (ZnCl₂) and Titanium Tetra Isopropoxide (TTIP). All the chemicals were analytical grade and were utilized exactly as they were given to us.

2.2. Synthesis of PANI/CdS–PANI/CdS–ZnS–PANI/CdS–TiO₂–PANI Nano Composites

PANI was created via a chemical technique that involved oxidizing aniline in H₂SO₄ with the aid of APS (Ammonium Persulphate). The color of the solution changed from pale to blue-green and turned to dark green by adding ammonium persulphate to it, indicating that polymerization of aniline into polyaniline occurs swiftly. The operations

were performed at low temperatures for the delayed process of polymerization to create the particles in nanosize. The following steps were used to make PANI and its different nanocomposites.

2.3. Preparation of Polyaniline (PANI)

In 100 mL chloroform, a 0.2 M aniline solution was produced (2.462 M). In 100 mL H_2SO_4 , another APS (0.05 M) solution was produced (1 M) and progressively mixed with the initial solution to polymerize overnight at 4–5 °C.

2.4. Preparation of CdS-PANI Nanocomposite (PC)

PC was made by using a single pot chemical precipitation process to in situ polymerize PANI in CdS nanoparticles. With vigorous stirring, a 100 mL aqueous solution of $\text{Cd}(\text{NO}_3)_2$ (0.085 M) was made and mixed with 50 mL methanol (24.44 M). A 100 mL aniline (0.2 M) solution produced in chloroform (2.462 M) was further mixed with this and stirred for another 60 min. The process was performed for 1 min in an H_2S environment with vigorous stirring and then continued for another 2 h. In a separate vessel, a 0.05 M APS solution was produced in 100 mL H_2SO_4 (1 M). This solution was progressively added to the preceding one and left to polymerize overnight at 4–5 °C. The finished product was a dark green color.

2.5. Preparation of CdS-ZnS-PANI Nanocomposite (CZP)

With continuous stirring, 50 mL methanol (24.44 M) was dropped into 100 mL aqueous ZnCl_2 (0.15 M). The stirring process was performed for 1 min in an H_2S environment and then followed for about another 2 h, resulting in the change in color to milky white. In a separate beaker, 100 mL aqueous $\text{Cd}(\text{NO}_3)_2$ (0.085 M) was added dropwise to 50 mL methanol (24.44 M) using a magnetic stirrer. The process was continued by stirring for 1 min in an H_2S environment and then followed for another 2 h. The color of the solution changed from clear to bright yellow. The two solutions were mixed vigorously for 2 h with vigorous stirring. The solution that resulted was yellow. Next, 100 mL aniline (0.2 M) solution produced in chloroform (2.462 M) was mixed with this reaction mixture and carried out for another 1 h using the stirring method. In a separate vessel, a 0.05 M APS solution was produced in 100 mL H_2SO_4 (1 M). This solution was progressively added to the preceding one and left to polymerize overnight at 4–5 °C. The finished product was a dark green color.

2.6. Preparation of CdS-TiO₂-PANI Nanocomposite (CTP)

In a typical synthesis, 100 mL aqueous $\text{Cd}(\text{NO}_3)_2$ (0.085 M) was added dropwise with continuous stirring, followed by 50 mL methanol (24.44 M) for 1 min in an H_2S environment using a magnetic stirrer and then followed the same for another 2 h. The color of the solution changed from clear to yellow. Then, 3.53 mL TTIP (Titanium Tetra Isopropoxide) (0.1 M) was mixed in the dropwise manner to this solution (20 drops per minute), followed by 2 h of stirring. The hue of the solution changed to a faint yellow. Then, 100 mL aniline (0.2 M) solution produced in chloroform (2.462 M) was dropped into this reaction mixture and stirred for 1 h. In a separate vessel, a 0.05 M APS solution was produced in 100 mL H_2SO_4 (1 M). This solution was progressively added to the preceding one and left to polymerize overnight at 4–5 °C. The finished product was a dark green color. Before drying in the air, all the precipitates were washed numerous times with water and acetone.

2.7. Characterization Techniques

Energy-dispersive X-ray spectroscopy (EDS, JEOL, JSM6510LV, Tokyo, Japan) and Fourier Transform Infrared Spectroscopy were used to examine element analysis (Spectrum 2, PerkinElmer, Waltham, MA, USA). Scanning Electron Microscopy (JEOL, JSM6510LV, Tokyo, Japan) and Transmission Electron Microscopy are used to characterize surface

morphology (JEOL, JEM2100, Tokyo, Japan). Powder X-ray diffraction (Miniflex-TM II Benchtop, Rigaku Co-operation, Tokyo, Japan) was used to examine the structural properties. Thermal Gravimetric Analysis was used to determine thermal properties (TGA). UV-Visible Spectroscopy was used to determine the optical properties (Shimadzu UV-1601, Waltham, MA, USA).

2.8. Photocatalytic Experiment

PANI and its nanocomposites (PC, CZP, and CTP) were used in photocatalytic tests to decolorize the dye derivative Acid Blue-29 (AB-29) in visible light. The inner and outer jackets of a standard immersion well photoreactor were employed. A halogen liner lamp was used for irradiation (500 W, 9500 Lumens). In the photocatalytic experiment, 180 mL of the dye solution with the concentration of 0.06 mM and the optimized catalyst dosage (1 gL^{-1}) was stirred in the shady for at least 20 min in the presence of atmospheric oxygen to achieve adsorption–desorption equilibrium between dye and catalyst surface. The initial phase (5 mL) of the solution (0 min) was then removed, and irradiation began. During the irradiation, further sections of samples (5 mL each) were collected at regular intervals and evaluated after centrifugation. Changes in absorption were used to track the decolorization of AB-29 using a UV-vis spectroscopic analysis approach (Shimadzu UV-Vis 1601). The dye concentration was determined using a standard calibration curve based on the dye's absorbance at various known values. It is critical to assess the catalyst's stability and reuse it to put it into practice. The photocatalytic capabilities of the nanomaterials were investigated for five consecutive cycles under similar conditions, using the same amount of catalyst nanomaterials and a fresh solution of dye sample each time.

3. Results and Discussion:

3.1. Fourier Transform Infrared (FTIR) Spectroscopy

The FTIR analysis was used to determine the vibrational modes in PANI and its composite nanomaterials (PC, CZP, and CTP), as well as to investigate the interaction of capping molecules with the surfaces of conducting polymers and nanoparticles. Figure 1 depicts the FTIR spectra of polyaniline and its nanocomposites from a scale of 4000 cm^{-1} to 400 cm^{-1} . The bands at 3460 cm^{-1} and 3230 cm^{-1} correspond to free (non-hydrogen bonded) NH stretching vibrations and hydrogen-bonded NH bonds between amine and imine sites, respectively [54,55]. The C=C bond stretching vibration peak in the quinone, and benzene ring was at 1572 cm^{-1} and 1497 cm^{-1} , respectively [56], the C-N bond stretching vibration peak in the quinone ring and benzene ring was at 1301 cm^{-1} , and 1245 cm^{-1} , respectively [57]. Peaks observed in the $1000\text{--}1200 \text{ cm}^{-1}$ range were caused by aromatic in-plane C-H bending modes [58]. The band at 1173 cm^{-1} was thought to be strong and was used to determine the electron delocalization, so it is a PANI conductivity characteristic peak [55]. C-H deformations in the 1,4-disubstituted benzene ring were discovered at 870 cm^{-1} [59]. The FTIR spectra of synthesized PANI matched previous findings [60].

The characteristic peak for CdS in the FTIR spectra for PC was 405 cm^{-1} [61,62]. Some PANI peaks shifted as a result of the addition of CdS nanoparticles. When compared to the pure PANI peak at 3460 cm^{-1} , the band corresponding to polyaniline at 3506 cm^{-1} shifted blue, and for pure PANI peak at 1561 cm^{-1} , 1489 cm^{-1} , 1298 cm^{-1} , 1245 cm^{-1} , 1126 cm^{-1} , and 813 cm^{-1} shifted red and progressively moved to 1548 cm^{-1} , 1451 cm^{-1} , 1290 cm^{-1} , 1243 cm^{-1} , 1119 cm^{-1} , and 784 cm^{-1} . The appearance of the band at 1119 cm^{-1} in the nanocomposite indicated the production of polyaniline [55–58]. CdS and Polyaniline established a coordination bond in PC, resulting in weaker bonds and vibrations and the conjugated system of PANI. This resulted in a higher density of electrons in CdS and, as a result, a higher number of photoelectrons, resulting in greater photocatalytic activity of nanocomposites [54]. In addition, CZP has redshift at 1555 cm^{-1} , 1475 cm^{-1} , 1287 cm^{-1} , 1227 cm^{-1} , 1108 cm^{-1} , and 807 cm^{-1} , attributing to pure Polyaniline, representing reduced conjugated system and bond strengths of polyaniline, as well as enhanced electron density

in CdS, indicating higher photocatalytic activity of CZP. The absorption bands at 405 cm^{-1} and 612 cm^{-1} showed the existence of CdS [52,62] and ZnS [63,64] in CZP, correspondingly. The Ti-O and O-Ti-O bonds in TiO_2 were responsible for the broad CTP peaks around $400\text{--}800\text{ cm}^{-1}$ [55,60]. This broad peak coincided with PANI's high of 813 cm^{-1} and CdS typical peak of 405 cm^{-1} . The characteristic bending mode of water molecules adsorbed on TiO_2 surface caused the band intensity at 1629 cm^{-1} in CTP nanocomposite [60]. The existence of a peak at 1139 cm^{-1} in CTP [55] confirmed the development of PANI. Some PANI peaks shifted due to the inclusion of TiO_2 particles. The peaks at 3426 cm^{-1} , 3079 cm^{-1} , 1560 cm^{-1} , 1486 cm^{-1} , 1290 cm^{-1} , and 1238 cm^{-1} , displaced to lower wavenumbers (red-shift), were weak after coupling with TiO_2 [60]. As a result, the density of electrons in TiO_2 rose, and the photocatalytic activity of CTP improved.

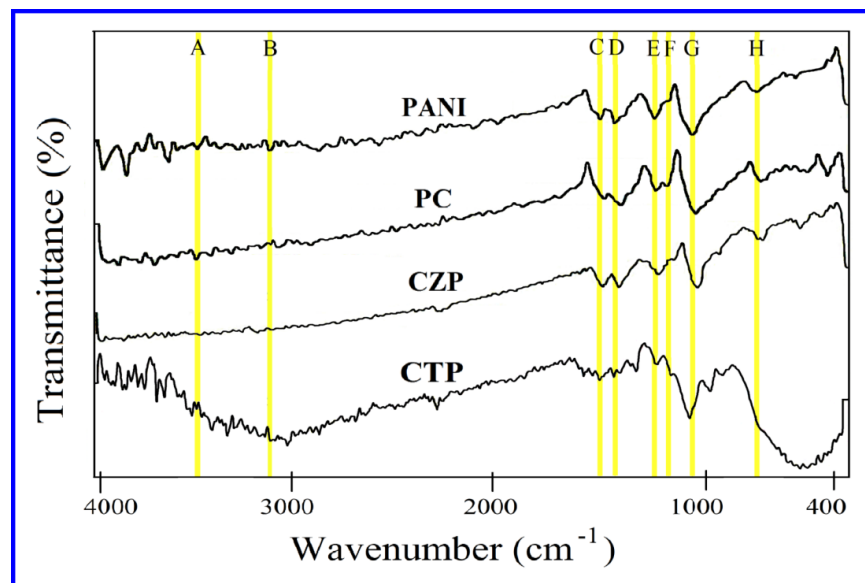


Figure 1. FTIR spectra of PANI, PC, CZP and CTP nanocomposites.

3.2. Energy Dispersive X-ray Spectroscopy (EDS)

The EDS spectra of PC, CZP and CTP nanocomposites are shown in Figure 2. The graphs revealed the presence of carbon, oxygen, sulfur, zinc, titanium, and cadmium, which was expected. Peaks of CdS in PC, CdS and ZnS in CZP, and CdS and TiO_2 in CTP all demonstrate that necessary semiconductors are present in Polyaniline.

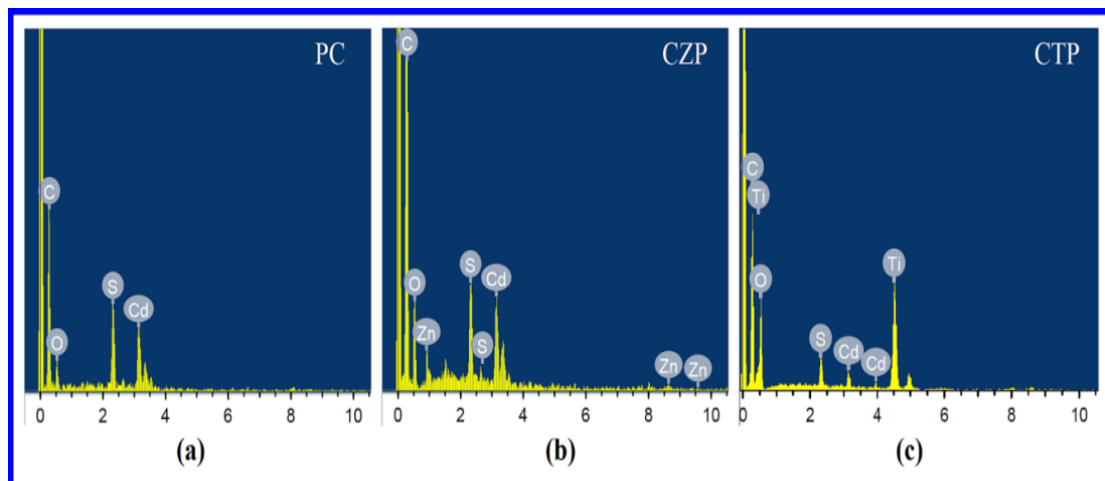


Figure 2. EDS spectra of (a) PC, (b) CZP and (c) CTP.

3.3. Scanning Electron Microscopy (SEM)

Surface morphologies of the PANI, PC, CZP, and CTP nanocomposites are displayed in Figure 3. According to the SEM pictures, the catalysts contain a combination of agglomerated and non-agglomerated fluffy particles, which is consistent with previous findings [54]. In CTP nanocomposites, some surface-residing nanoparticles can be visible, but they are not evenly dispersed. From the SEM images, no apparent pores were seen on the membranes' surface. The sub-layers of PANI, PC, CZP, and CTP appear to be slightly porous, while the top layer appears to be fully compact. When compared to the PANI, which has a few large pores, CTP and PC contain a lot of small pores.

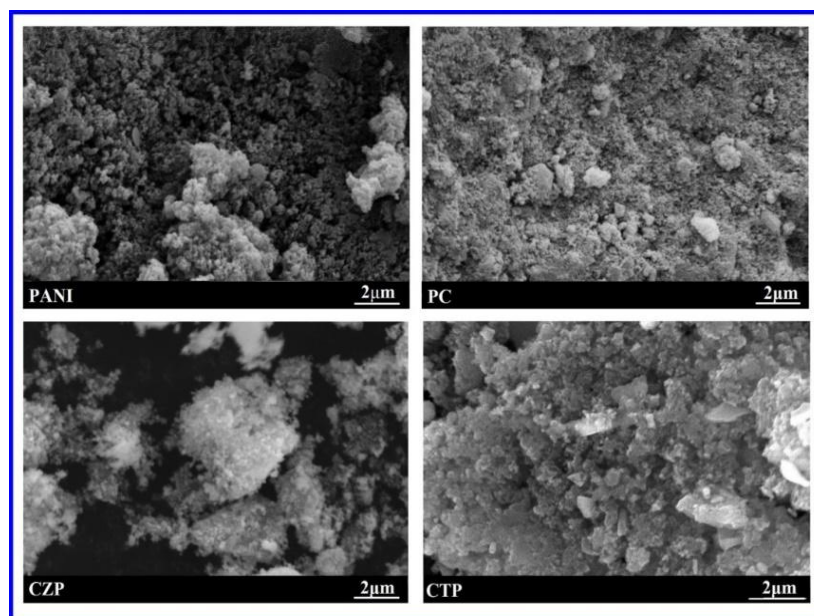


Figure 3. SEM images of PANI, PC, CZP and CTP nanocomposites.

3.4. Transmission Electron Microscopy

TEM images of synthesized polyaniline nanostructures are shown in Figure 4a,b (PANI). It was possible to see a huge number of interconnected branched polyaniline nanofibers. Most fibers had diameters of less than 50 nm. TEM images of PC are shown in Figure 4c. On the PANI nanofibers, homogenous spherical CdS nanoparticles were found to be well disseminated. The presence of CdS in PANI had previously been established using FTIR and EDS. It was discovered that the presence of PANI in the composites reduced the aggregation of CdS particles to some extent. As previously stated for PC, this allowed for simple electron transport from PANI to CdS, as well as easily activated photoelectrons in CdS, resulting in increased photocatalytic efficiency for dye degradation of PC. Figure 4d shows a representative diagram of a PC.

The two distinct-sized spherical nanoparticles distributed in the PANI matrix were observed and revealed by TEM images of CZP (Figure 5a,b). As demonstrated by EDS and FTIR, the generation of CdS and ZnS Sandwich type (SW-type) quantum dots (QDs) was confirmed by two different sizes and spherical structures. CdS and ZnS were found close with one another in the polymer matrix, implying the strongest bonding connecting each other, as demonstrated by FTIR. Figure 5 shows a sample schematic of CZP (c). Similarly, CTP TEM images (d) and (e) indicated two different sized CdS and TiO₂ QDs on the surface of the PANI matrix. Figure 5 depicts a sample diagram of CTP (f). Two different-sized spherical nanostructures appeared to be nearest, as suggested by EDS and FTIR, supporting the production of CdS and TiO₂ SW-type NCs in the polyaniline matrix with significant bonding among each other. A typical schematic of CTP is shown in Figure 5f.

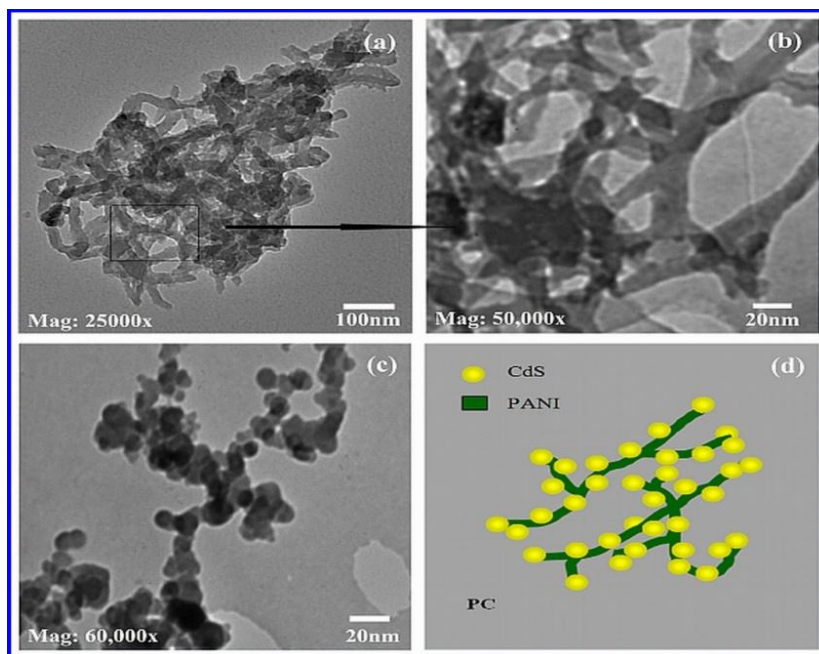


Figure 4. TEM images of (a) PANI at 25,000 times magnification, (b) PANI at 50,000 times magnification, (c) PC at 60,000 times magnification and (d) representative diagram of PC.

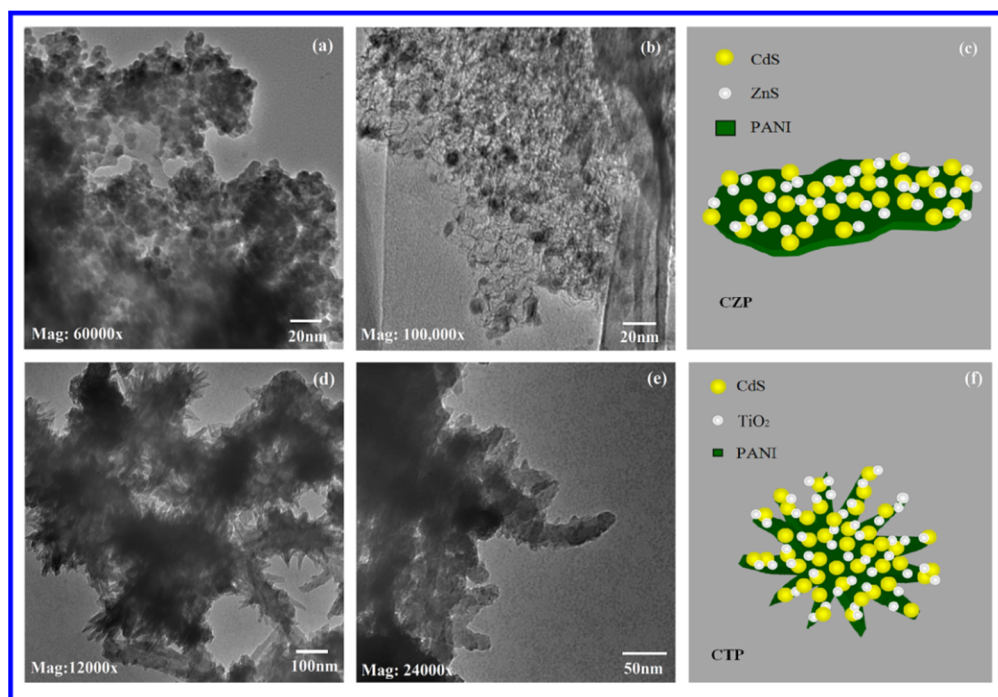


Figure 5. TEM images of (a,b) CZP at 60,000- and 100,000-times magnification, respectively, (d,e) CTP at 12,000- and 24,000-times magnification, respectively and (c,f) representative diagrams of CZP and CTP, respectively.

3.5. X-ray Diffraction (XRD) Spectroscopy

Figure 6a shows the powder XRD patterns of PANI, PC and CdS. The characteristic broad peak of amorphous PANI centered at $2\theta = 25^\circ$ was observed in the figure [65]. The production of cubic CdS QDs embedded in PANI was suggested by the diffraction patterns corresponding to PC, which had peaks comparable to cubic CdS centered at $2\theta = 25.955^\circ$ (111), 29.428° (200), 43.372° (220), and 51.395° (311) [66]. The XRD peaks for PC were a

little wider than expected, which could be attributed to the inclusion of PANI. The Scherrer formula [67,68] was used to compute the predicted crystal size of CdS, which came out to be 6.4 nm. Figure 6b shows the XRD pattern of CZP. The XRD pattern is centered at $2\theta = 24.471^\circ, 26.018^\circ, 27.740^\circ, 36.093^\circ, 43.458^\circ, 47.645^\circ$ and 51.507° belonging to hexagonal ZnS ($2\theta = 24$ (100), 26 (002), 27 (101), 36 (102), 43 (110), 47 (103) and 51 (112)) [69,70] and cubic CdS with characteristic peaks at $2\theta = 26^\circ$ (111), 29° (200), 43° (220), and 51° (311) [36,54,66]. The XRD spectra revealed significant widening due to PANI. The crystal size of CZP was impossible to quantify due to the overlap of the peaks respective to the nanocomposites used for the catalysis process. Figure 6c shows the XRD spectrum of CTP. At $2\theta = 25^\circ$, a broad peak was discovered, as the combination of anatase TiO₂, cubic CdS, and polyaniline. The Peaks at $2\theta = 37.8^\circ$ (103), 48.07° (200), 54.18° (105), 62.42° (204) and 75.2° (215) corresponds to anatase TiO₂ [71], while peaks at 29.239° (200), 43.372° (220) and 51.395° (311) were associated with cubic CdS [36,54,66]. Because of the existence of the nanocomposite peak which is used as the photocatalyst, the crystalline size was not able to deduct.

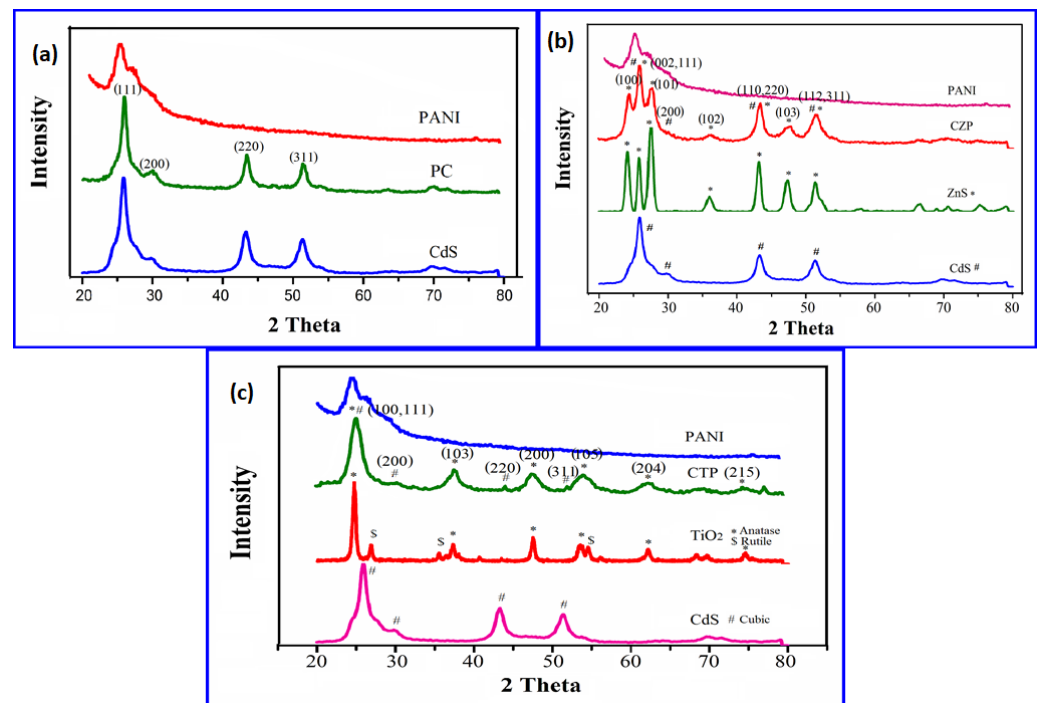


Figure 6. (a) XRD pattern of PC in comparison to cubic CdS and synthesized PANI (b) XRD pattern of CZP in comparison to cubic CdS, hexagonal ZnS and PANI (c) XRD pattern of CTP in comparison to cubic CdS, Degussa P-25 TiO₂ and PANI.

3.6. Thermal Analysis

The decrease in weight was seen in the TGA thermograph of PANI at two temperatures in the range from 30 to 100 °C as shown in Figure 7. The sample's first mass loss began at 20 °C and rapidly ended at 100 °C. The evaporation of absorbed moisture, the removal of contaminants, residual water, and unreacted monomers all contribute to this effect, which can be seen in a variety of polymers. The polymer breakdown started at around 210 °C (the most commonly quoted was around 300 °C) [36,65]. At 800 °C, the degradation was quite moderate, and the observed mass loss was not significant, since it did not surpass 46%. The heat resistance of the synthesized polyaniline was found to be above average in this study.

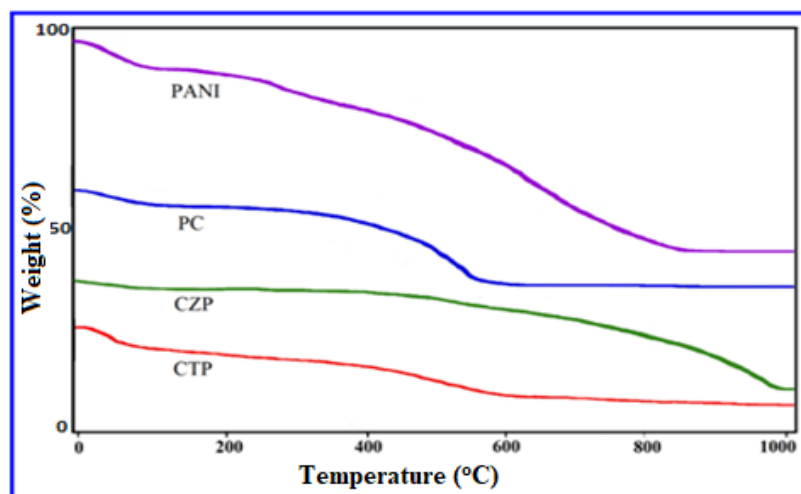


Figure 7. TGA curves of PANI, and its composite nanomaterials (PC, CZP, and CTP).

The stability was increased by the decomposition at high temperature for the sample in the TGA profile [56] compared to pure PANI (280–300 °C) and consistent thermal stability from 600 °C to 1000 °C. It could be related to the use of CdS nanoparticles in the polymer matrix, which resulted in a higher binding force due to CdS nanoparticle interaction with the lone pair electrons of the N atom in the polymer backbone. The primary weight loss peak in CZP was discovered at a significantly elevated temperature (400 °C) (which begins at about 280–300 °C) and persisted for the composites up to 980 °C, demonstrating greater composite stability due to inorganic semiconductor nanoparticles [56]. TGA curve of CTP's also revealed a rise in the second-stage breakdown temperature to 420 °C, as well as consistent thermal stability between 600 °C and 1000 °C. At 20–80 °C, the sample began to lose mass due to moisture, contaminants, and unreacted monomers. The presence of a significant association between PANI and CdS-TiO₂ could explain the CTP nanocomposite's increased thermal stability when compared to pure PANI.

3.7. Optical Analysis

Figure 8a–d shows the UV-visible absorption spectra of PANI, PC, CZP, and CTP nanocomposites, respectively. The optical characteristics of the sample in N-methyl pyrrolidinone (NMP) solution were measured using a UV-Vis Spectrometer. NMP is a non-protonating polyaniline solvent that is extremely rare [65]. The absorption spectra of PANI (Figure 8) revealed two absorption peaks at 320 nm and 630 nm, which correspond to the polyaniline emeraldine base form. The excitation of benzenoid ring was attributed to the intensity band at 320 nm, while the absorption at 630 nm was attributed to a benzenoid to quinoid excitonic transition [72,73]. The existence of typical peaks of π - π^* transitions (at $\lambda = 420$ – 450 nm and 760 – 800 nm) without any indications of transitions involving polarons showed that the prepared polyaniline was due to the emeraldine base form of polyaniline [65]. Figure 8b depicts the absorption spectra of PC. PC had two prominent peaks at 320 nm and 630 nm, with one hump at 420 nm, in its absorption spectra. The π - π^* transition in the benzenoid ring and the benzenoid to quinoid excitonic transition of polyaniline were attributed to the peaks at 320 nm and 630 nm, respectively, indicating emeraldine base type polyaniline. CdS QDs were responsible for the shoulder at 420 nm, which displayed a significant blue shift from the bulk (510 nm) [74]. As a result, there appears to be a substantial interaction between CdS and PANI. Figure 8c depicts the absorption spectrum of CZP. The spectrum indicated just two peaks centered at 340 and 620 nm, with the strength of the spectrum increasing compared to pure PANI. Some authors [75] report a rise in the peak intensity corresponding to polyaniline in addition to the semiconductor nanocomposites. The appearance of band intensity at 340 and 620 nm has corresponded to the emeraldine base type of the PANI matrix. Instead of the peaks attributing to CdS

(512 nm) [74] and ZnS (336 nm) [76], the peak at 340 nm displayed broadening from 280 to 350 nm with a tail in the visible region up to 400 nm, demonstrating the strong bonding of CdS and ZnS nanoparticles with polyaniline. PANI's absorption spectrum revealed a blue shift in the presence of the CdS-ZnS nanocomposite without revealing any extra peaks, and the augmentation in the absorption spectrum was analyzed because of the significant interaction [59,75]. An improved photoresponse was predicted in comparison to pure PANI and CdS-ZnS sandwich nanocomposite. Figure 8d depicts the absorption spectrum of CTP. CTP's absorption spectrum revealed two large peaks at 330 nm and 640 nm, as well as a faint broad peak at 450 nm. The absorption intensity of the CTP spectra was reduced when compared to pure PANI. CdS QDs were responsible for the faint peak at 450 nm, while emerald base polyaniline was responsible for the peaks at 330 and 640 nm. Colloidal TiO₂ nanoparticles' absorption overlapped with polyaniline, which caused the peak at 330 nm to grow dramatically from 290 to 350 nm, with a tail in the visible region up to 400 nm. The blue shift and decrease in intensity of the CTP revealed a significant interaction of quantum dots (CdS and TiO₂) and PANI [59]. CTP may be activated through the absorption of UV and visible light (between 190 and 800 nm), which is an excellent choice for photocatalytic applications.

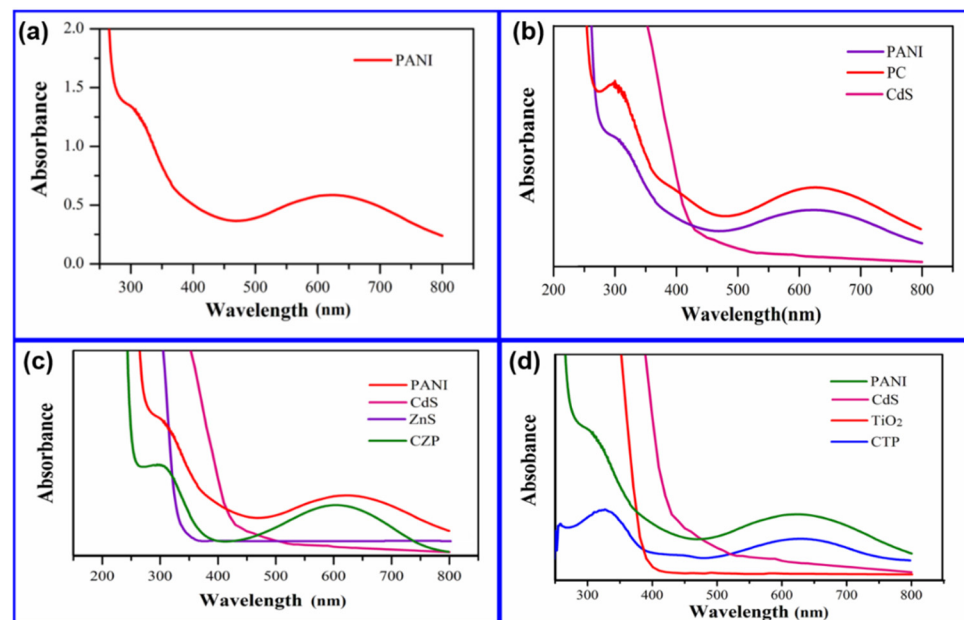


Figure 8. (a) UV-visible spectra of PANI in the range 200 to 800 nm (b) UV-visible spectra of PC in comparison to bulk CdS and synthesized PANI. (c) UV-visible spectra of CZP in comparison to bulk CdS and ZnS and synthesized PANI. (d) UV-visible spectra of CTP in comparison to synthesized PANI, bulk CdS and ZnS.

3.8. Photocatalytic Activity:

Acid blue dye was used to test the photocatalytic activity of CdS, CdS-ZnS, and CdS-TiO₂ nanoparticles mounted on PANI membranes (AB-29).

3.8.1. Photocatalysis by PC

The photocatalytic response of PC is depicted in Figure 9a–d. Our results showed that while PANI had only a minor effect on photocatalyst activity, it was beneficial for improving photocatalyst stability. PC demonstrated better photocatalytic degradation activity compared to pure CdS and PANI. The reasons for PC's improved photocatalytic activity are as follows: first, the density of the photoelectrons in CdS was increased by the transfer of photoexcited electrons. Second, the separation of the charges and the charge density were increased by the attraction of all the holes from CdS by PANI. Third, the addition of CdS caused some order to the disordered structure of PANI, and PANI

prevented some agglomeration and size growth of CdS particles, resulting in efficient and rapid photodegradation of adsorbed contaminants [77]. The relative change in the concentration (C/C_0) of AB-29 is shown in Figure 9a with and without the catalysts (PC, PANI, and pure CdS NP). After 90 min of irradiation decolorization of AB-29 was 82.2%, 69.8%, and 67.1%, respectively, as shown in Figure 9a. In the absence of photocatalyst, however, there was no discernible decrease in dye concentration. The decolorization curve (Figure 9a) indicated a pseudo-first-order response, which was also shown in Figure 9b. The slope of $\ln(C_0/C)$ versus t will be k_{app} . For all of the studies, the correlation constant (R^2) for the fitted lines was calculated to be around 0.99. The decolorization rate ($\text{molL}^{-1}\text{min}^{-1}$) of AB-29 was calculated using the rate constant obtained from Figure 9b. The computed rates ($\text{molL}^{-1}\text{min}^{-1}$) were 4.47×10^{-4} (PANI), 4.62×10^{-4} (CdS), and 5.54×10^{-4} (PC). Figure 9c depicts the decolorization rate of AB-29 breakdown of several photocatalysts (PC, PANI, and pure CdS NP). It was critical to assess the catalyst's stability and reuse to put it into practical usage. The photodegradation of AB-29 during five successive cycles with the same 1 gL^{-1} catalyst at 0.06 mM dye concentration is shown in Figure 9d. Before each photocatalytic run, the nanocomposite catalyst was rinsed with double distilled water after each cycle and a fresh solution of AB-29 was added. After 90 min of reaction time, the relative decolorization utilizing PC for the 5-cycling reuse was 82.3%, 81.8%, 81.6%, 81.1%, and 80.8%, respectively. The catalytic activity of PC reduced little following the first cycles, whereas the activity of pure CdS decreased dramatically. The runoff from the PC while washing and filtering could be the cause of this minor movement. However, in subsequent studies, the decolorization efficiency remained rather constant, indicating that CdS QDs were consistently mixed within the PANI matrix. In this regard, the recycle of PC photocatalyst confirmed the PC's relative stability. As a result, PC appears to be a superior photocatalyst to pure CdS and PANI, with increased activity and stability.

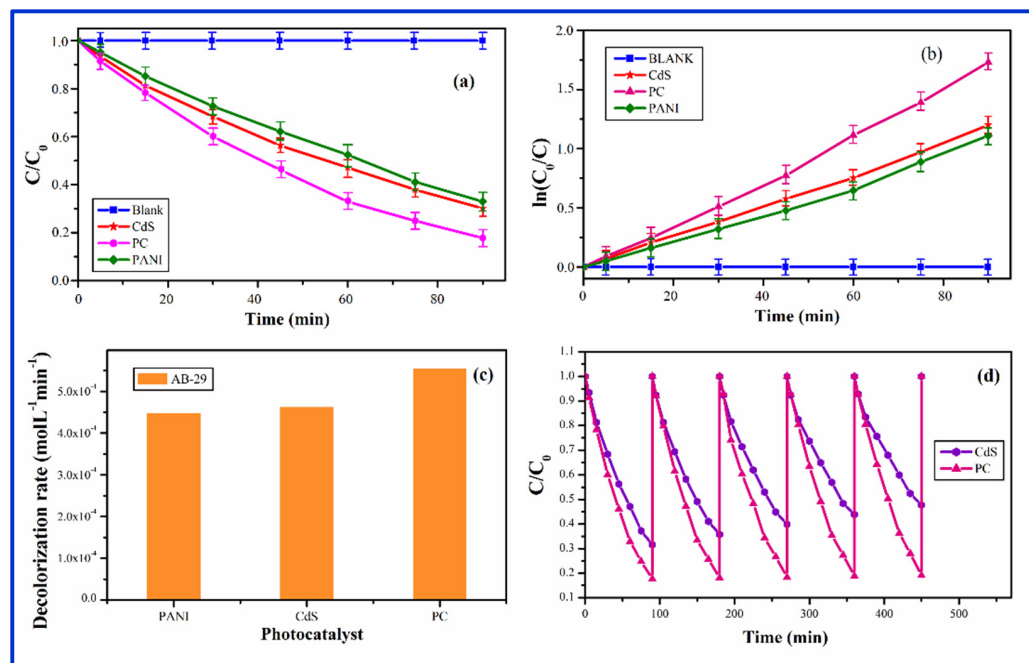
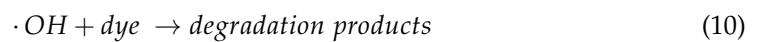
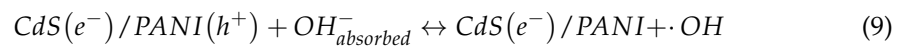
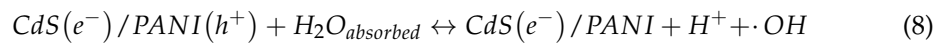
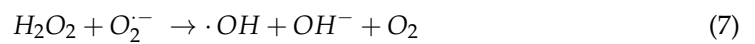
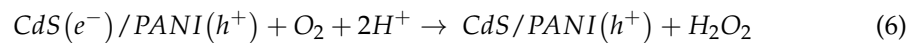
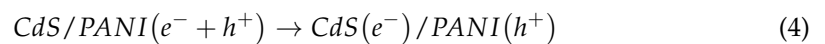
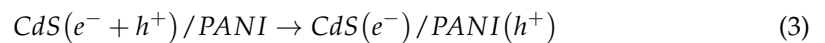
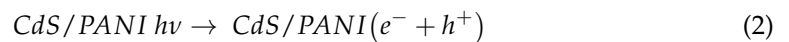
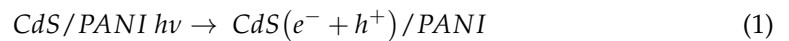


Figure 9. (a) Change in concentration of AB-29 with time in the presence and absence of PC in comparison to PANI and CdS nanoparticles. (b) Change in concentration of AB-29 with time in the presence and absence of PC in comparison to PANI and CdS nanoparticles. (c) The decolorization rate of AB-29 in the presence of synthesized PC in comparison to PANI and CdS nanoparticles. (d) Stability and recycle of PC in comparison to pure CdS.

Electrons were scavenged by molecular oxygen O_2 in oxygen-equilibrated environments, resulting in the superoxide radical anion $\text{O}_2^{\cdot-}$. (Equation (5)) and hydrogen perox-

ide H_2O_2 (Equation (6)). These newly formed intermediates combined to form the hydroxyl radical $\cdot\text{OH}$ (Equation (7)). The photo-generated hole at PANI oxidized the hydroxyl groups (OH) (Equation (8)) and the water (H_2O) molecule (Equation (9)), resulting in hydroxyl radicals ($\cdot\text{OH}$). The $\cdot\text{OH}$ radical, which is a powerful oxidizing agent capable of degrading a wide range of contaminants, played a role in the degradation of the dye AB-29 (Equation (10)) [77,78].

The reactions can be expressed as follows:



3.8.2. Photocatalysis by CZP

Figure 10a–d show the photocatalytic response of CZP in comparison to pure CdS, ZnS, and PANI. CZP had higher photocatalytic degradation activity than pure CdS, ZnS, PANI, and CdS-ZnS NC. In Figure 10a, the relative change in concentration (C/C_0) of organic dye AB-29 was plotted as a function of time with and without photocatalysts (CZP, PANI pure CdS, and ZnS QDs, and CZS-ZnS NC). When compared to pure CdS or pure PANI, CZP demonstrated a significant increase in photoactivity, but only a minor increase when compared to CdS-ZnS NC. Although PANI only slightly increased the catalytic efficiency of CdS-ZnS NC (in CZP), it was discovered to be more beneficial for improving photocatalyst stability when compared to pure CdS-ZnS NC in the absence of polyaniline, as polyaniline reduced CdS photo corrosion by attracting all holes to itself. The decolorization of AB-29 after 90 min of irradiation with CZP, pure CdS-ZnS NC, CdS QD, PANI, and ZnS QD was 89.8 percent, 86.5%, 69.8%, 67.1%, and 14.2%, as shown in Figure 10a. The decolorization curve (Figure 10a) suggested a pseudo-first-order response, which was confirmed by plotting $\ln(C_0/C)$ vs. irradiation time in Figure 10b. The correlation constant (R^2) for the fitted lines was calculated to be around 0.99 for all the studies. The rate constant obtained from Figure 10b was used to compute the decolorization rate ($\text{molL}^{-1}\text{min}^{-1}$) of AB-29. The computed decolorization rates for ZnS, PANI, CdS, CdS-ZnS, and CZP were $0.89 \times 10^{-4} < 4.47 \times 10^{-4} < 4.62 \times 10^{-4} < 5.63 \times 10^{-4} < 5.84 \times 10^{-4} \text{molL}^{-1}\text{min}^{-1}$, respectively. Figure 10c depicts the decolorization rate of AB-29 breakdown with several photocatalysts (ZnS, PANI, CdS, CdS-ZnS and CZP). Figure 10d depicts the photodegradation of AB-29 during a five-cycle period. After 90 min of reaction time, the relative decolorization utilizing CZP for the 5-cycling reuse was 89.8%, 88.9%, 88.0 percent, 87.9%, and 87.1%, respectively. The photocatalytic activity of CZP reduced slightly after the first cycles, compared to pure CdS-ZnS NC in the absence of polyaniline the catalytic activity was reduced dramatically (74.5%, 71.5%, 67.1%, 61.8% and 53.5%). The CZP runoff during washing and filtering could be the cause of this modest drop. However, in subsequent experiments, the decolorization efficiency remained rather constant. The recycling of CZP photocatalyst confirmed the relative stability of the CZP in this regard. As a result, CZP appears to be a superior photocatalyst to pure CdS-ZnS in terms of activity and stabil-

ity [79]. Figure 11 depicts a schematic representation of the CZP mechanism, which involves photoexcited electrons and holes.

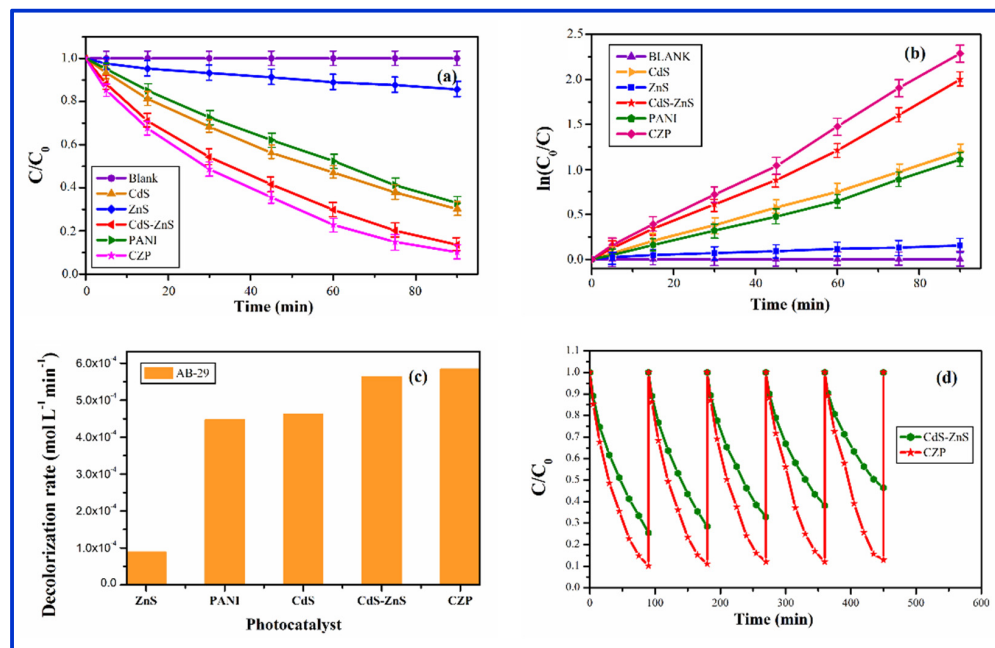


Figure 10. (a) Change in concentration of AB-29 with time in the presence and absence of CZP in comparison to PANI, CdS and ZnS nanoparticles and CdS-ZnS nanocomposite (b) Change in concentration of AB-29 with time in the presence and absence of CZP in comparison to PANI, CdS and ZnS nanoparticles and CdS-ZnS nanocomposite (c) The decolorization rate of AB-29 in the presence of synthesized CZP in comparison to PANI, CdS and ZnS nanoparticles and CdS-ZnS nanocomposite (d) Stability and recycle of CdS-ZnS nanocomposite embedded in PANI (CZP), in comparison to free CdS-ZnS nanocomposite without PANI.

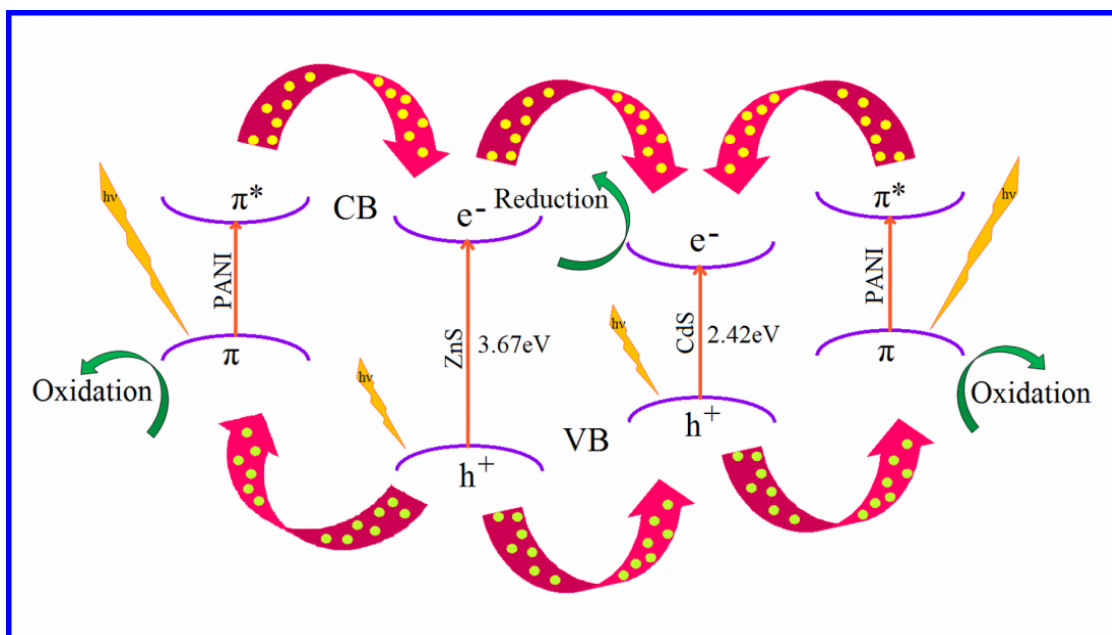
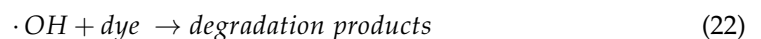
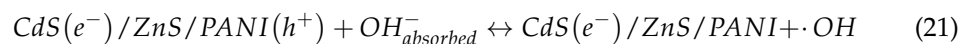
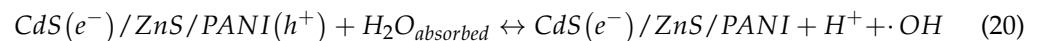
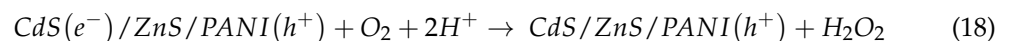
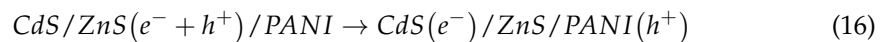
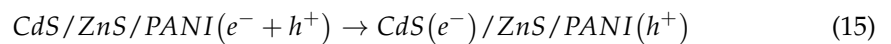
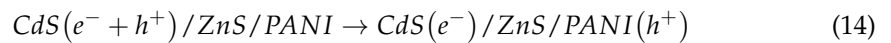
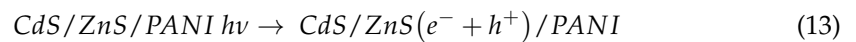
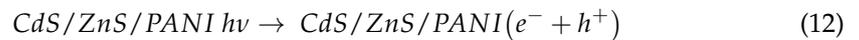
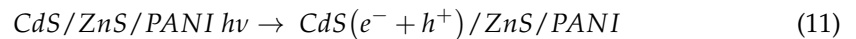


Figure 11. Representative diagram of the mechanism of photocatalysis by CZP.

The following are examples of reactions:



3.8.3. Photocatalysis by CTP

The photocatalytic performance of CdS-TiO₂ nanocomposites on polyaniline is shown in Figure 12a–d. CTP outperformed pure CdS, TiO₂, PANI, and CdS-TiO₂ in terms of photocatalytic degradation (without PANI). In comparison to CdS-TiO₂, our findings showed that PANI had only a minor influence on CTP activity while significantly increasing CTP stability (CdS-TiO₂ NC in the absence of Polyaniline). It was feasible to push photogenerated charges by attaching TiO₂ and PANI to the surface of CdS, resulting in more effective charge separation in CTP [80]. Figure 12a depicts the relative change in concentration (C/C₀) of the organic dye AB-29 as a function of time, with and without photocatalysts (CTP, PANI pure CdS and TiO₂ QDs, and CdS-TiO₂) (CTP, PANI pure CdS and TiO₂ QDs, and CdS-TiO₂). As shown in Figure 12a, after 90 min of irradiation with CTP, CdS-TiO₂, CdS QD, PANI, and TiO₂ quantum dots, the decolorization of AB-29 was 86.4%, 83.2%, 69.8%, 67.1%, and 10.4%, respectively. However, the absence of the photocatalyst does not have any discernible reduction in the concentration of the dye. According to the photocatalytic results, CTP had a significant increase in photoactivity when compared to pure CdS, TiO₂, or pure PANI, but only a minor increase when compared to CdS-TiO₂ NC. The decolorization curve (Figure 12a) indicated a pseudo-first-order reaction, which was also demonstrated by plotting ln(C₀/C) versus irradiation time in Figure 12b. The correlation constant (R²) for the fitted lines was calculated to be around 0.99 for all of the studies. The rate constant obtained from Figure 12b was used to compute the degradation rate (molL⁻¹min⁻¹) of AB-29. The computed degradation rates for TiO₂, PANI, CdS, CdS-TiO₂, and CTP were 0.671 × 10⁻⁴ < 4.47 × 10⁻⁴ < 4.62 × 10⁻⁴ < 5.37 × 10⁻⁴ < 5.56 × 10⁻⁴ molL⁻¹min⁻¹, respectively. Figure 12c depicts the decolorization rate of AB-29 breakdown with several photocatalysts (pure TiO₂ QDs, PANI, CdS QDs, CdS-TiO₂ and CTP). The photodegradation of AB-29 during five consecutive cycles is depicted in Figure 12d. After 90 min of reaction time, the relative decolorization utilizing CTP for the 5-cycling reuse was 86.5%, 85.9%, 85.1%, 84.5%, and 83.8 %, respectively. Witnessing the outcome that the CTP's catalytic activity reduced slightly after the first cycles, whereas pure CdS-TiO₂ NC's activity decreased dramatically (83.3%, 79.5%, 75.2%, 72.4% and 70.1%). The explanation for this drop could be due to CTP runoff during washing and filtering, which has a constant decolorization rate. The recycling of CTP photocatalyst confirmed the CTP's relative stability in this regard, which shows that polyaniline prohibited CdS from CTP from photocorroding, hence improving its stability. As a result, it can be stated that CTP is a superior photocatalyst to pure CdS-TiO₂ in terms of activity and stability.

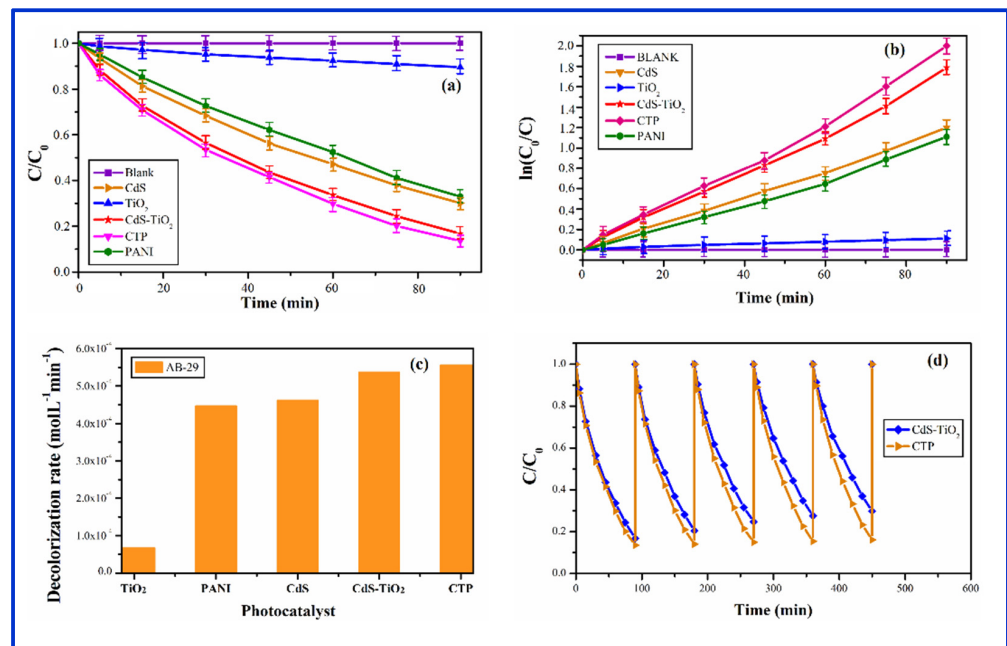


Figure 12. (a) Change in concentration of AB-29 with time in the presence and absence of CTP in comparison to PANI, CdS and TiO₂ nanoparticles and CdS-TiO₂ nanocomposite (b) Change in concentration of AB-29 with time in the presence and absence of CTP in comparison to PANI, CdS and TiO₂ nanoparticles and CdS-TiO₂ nanocomposite (c) The decolorization rate of AB-29 in the presence of synthesized CTP in comparison to PANI, CdS and TiO₂ nanoparticles and CdS-TiO₂ nanocomposite (d) Stability and recycle of CdS-TiO₂ nanocomposite embedded in PANI (CTP) in comparison to free CdS-TiO₂ nanocomposite without PANI.

Photo-excited electron-hole pairs were produced when CdS-TiO₂-PANI nanocomposites (CTP) were bombarded with visible light, which could explain the photocatalytic response of CZP. The mechanism using photogenerated charges of CTP is depicted schematically in Figure 13.

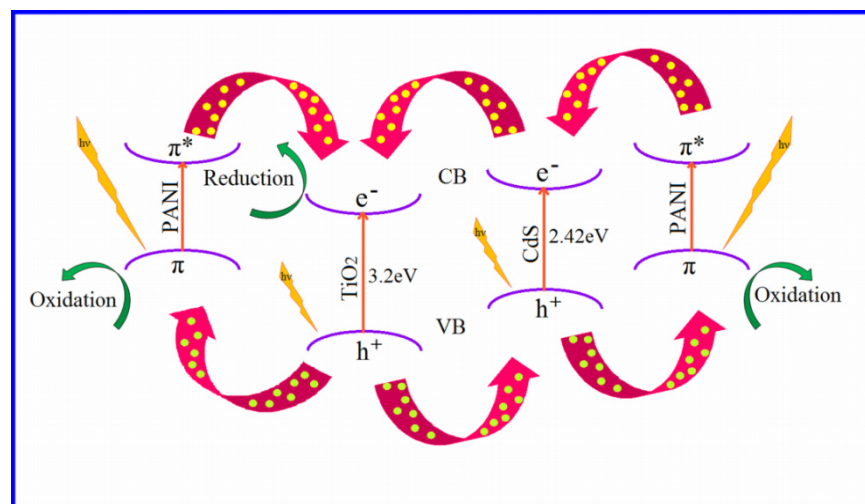
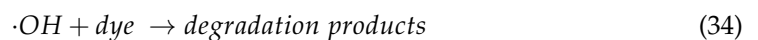
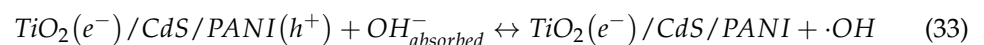
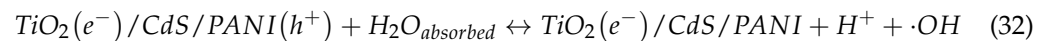
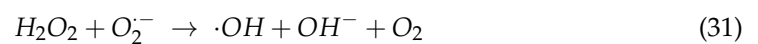
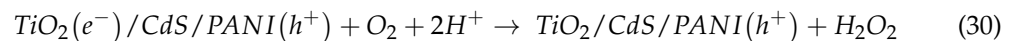
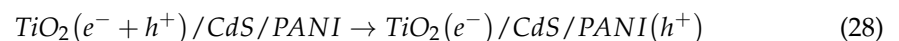
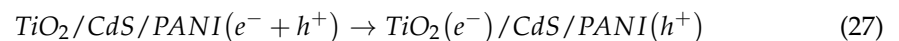
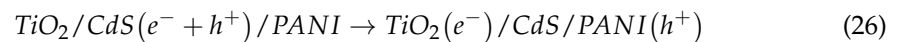
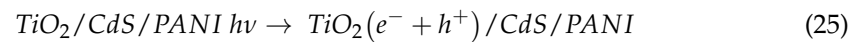
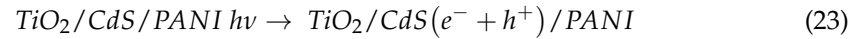


Figure 13. Representative diagram of the mechanism of photocatalysis by CTP.

In oxygen-equilibrated media, the electrons were scavenged by molecular oxygen O₂, resulting in the superoxide radical anion O₂^{•−} (Equation (29)) and hydrogen peroxide H₂O₂ (Equation (30)). The hydroxyl radical ·OH was produced when these newly created intermediates interacted (Equation (31)). The hydroxyl groups (OH) (Equation (32)) and

the water (H₂O) molecule (Equation (33)) were oxidized by the photo-generated hole at PANI, resulting in hydroxyl radicals ($\cdot\text{OH}$). The $\cdot\text{OH}$ radical behaved as a strong oxidizing agent, causing the dye AB-29 to deteriorate (Equation (34)). The process was articulated by the following equation:



Comparative Analysis: Table 1 represents the earlier reported work on the degradation of AB-29 dyes.

Table 1. Represents the comparison results of degradation of AB-29 dyes.

S.No.	Synthesized Material or Medium	Rate of Degradation (%)	Decolorization Rate (molL ⁻¹ min ⁻¹)	References
1.	Sulfuric acid-activated slug	95%		[81]
2.	Activated electric arc furnace slag	98%		[82]
3.	Zeolite/chitosan composite		The Langmuir monolayer adsorption capacities of the Z-AC/C composites are 212.76, 238.09, and 270.27 mg/g for AB29 at 30 °C, 40 °C, and 50 °C, respectively	[83]
4.	In the presence and absence of air by Fenton and Fenton-like processes using hydrogen peroxide (HP) and sodium persulfate (SPS), respectively, as oxidants	95.8% at pH 3 in 180 min.		[84]
5.	Montmorillonite K10-Cu(II)ethylenediamine (MMTK10-Cu(en)2)	83.27%		[85]
6.	In the presence/absence of sodium hydroxide (NaOH)	98% (in absence of NaOH)100% (in presence of NaOH)		[86]
7.	Polyaniline (PANI) with CdS (PC) PANI with CdS-ZnS (CZP) PANI with CdS-TiO ₂ (CTP)	82.2 89.8 89.8	5.54 × 10 ⁻⁴ 5.84 × 10 ⁻⁴ 5.56 × 10 ⁻⁴	Present Study

4. Conclusions

Semiconductor polyaniline nanocomposites were prepared using chemical precipitation method to increase the physical, chemical, optical and catalytic capabilities of semiconductors under ambient circumstances. The semiconductor nanoparticles were well

incorporated into the polyaniline matrix, which increased the thermal strength of PANI's and their optical and photocatalytic characteristics. PC stands for cubic CdS implanted on emeraldine base type polyaniline nanofibers in a CdS and PANI nanocomposite. The existence of CdS and ZnS in PANI was verified by EDX and FTIR. The frequency of the FTIR spectra was shifted to a lower value (redshift), which could be attributable to electron transfer from PANI to CdS and CdS-ZnS. XRD and UV-vis measurements both confirmed the cubic CdS and emeraldine base type Polyaniline. The thermal stability and optical properties of the PC have improved. PC also had better photocatalytic stability than pure CdS, implying that PANI decreased Cd²⁺ photo corrosion. CZP is a nanocomposite of CdS and ZnS embedded in PANI film. The microscopic examinations demonstrated that both the materials are close together in the PANI matrix, implying its development in Polyaniline. As a result, there appears to be substantial interaction between CdS-ZnS and PANI. CZP outperformed CdS-ZnS in terms of thermal stability, photocatalytic response, and stability. CTP is made up of CdS-TiO₂ nanocomposites that have been implanted in a PANI matrix. Cubic CdS and anatase TiO₂ were discovered in the XRD data. The presence of emeraldine base type Polyaniline was established by the UV-vis spectrum. Microscopic examinations revealed the presence of sandwich-type CdS-TiO₂ nanoparticles embedded in the PANI matrix. FTIR, XRD, UV-vis spectra and photocatalytic reaction all revealed a significant interaction between CdS-TiO₂ and PANI. By comparing pure with the CdS-TiO₂ nanocomposite, the photocatalytic efficiency was found to be more stable for up to five cycles. Although PANI has only a minor contribution to the photocatalytic activity of CdS and CdS-ZnS and CdS-TiO₂, we may conclude that it is advantageous for enhancing the stability of these nanomaterial photocatalysts. The photoactivity of the synthesized nanocomposites was found well within the visible region, hence this, along with improved stability, makes them suitable for commercial use under sunlight.

Author Contributions: N.Q.—Data curation, formal analysis, investigation, writing—original draft; P.S.—Writing—review & editing; S.S. (Suhail Sabir)—Formal analysis, Data curation; K.U.—Investigation; S.S. (Suresh Sagadevan)—Writing—review & editing. W.-C.O. Funding acquisition. All authors have read and agreed to the published version of the manuscript.

Funding: This research received no external funding.

Data Availability Statement: All relevant data are within the paper.

Conflicts of Interest: The authors declare no conflict of interest.

References

1. Tuzen, M.; Sari, A.; Saleh, T.A. Response surface optimization, kinetic and thermodynamic studies for effective removal of rhodamine B by magnetic AC/CeO₂ nanocomposite. *J. Environ. Manag.* **2018**, *206*, 170–177. [CrossRef] [PubMed]
2. Yao, Y.; Xu, F.; Chen, M.; Xu, Z.; Zhu, Z. Adsorption behavior of methylene blue on carbon nanotubes. *Bioresour. Technol.* **2010**, *101*, 3040–3046. [CrossRef] [PubMed]
3. Koysuren, O.; Koysuren, H.N. Photocatalytic activity of polyaniline/Fe-doped TiO₂ composites by in situ polymerization method. *J. Macromol. Sci. Part A* **2019**, *56*, 267–276. [CrossRef]
4. Preeti, S.; Abdullah, M.M.; Ikram, S. Role of Nanomaterials and their Applications as Photo-catalyst and Sensors: A Review. *Nano Res. Appl.* **2016**, *2*, 1.
5. Singh, P.; MAbdullah, M.; Sagadevan, S.; Kaur, C.; Ikram, S. Highly sensitive ethanol sensor based on TiO₂ nanoparticles and its photocatalyst activity. *Opt.-Int. J. Light Electron Opt.* **2019**, *182*, 512–518. [CrossRef]
6. Material Safety Data. Available online: https://biotech.bio5.org/sites/default/files/msds.Acid_Blue_29.pdf (accessed on 26 October 2009).
7. Saleh, T.A.; Tuzen, M.; Sari, A. Polyamide magnetic palygorskite for the simultaneous removal of Hg(II) and methyl mercury; with factorial design analysis. *J. Environ. Manag.* **2018**, *211*, 323–333. [CrossRef]
8. Saleh, T.A.; Adio, S.O.; Asif, M.; Dafalla, H. Statistical analysis of phenols adsorption on diethylenetriamine-modified activated carbon. *J. Clean. Prod.* **2018**, *182*, 960–968. [CrossRef]
9. Xiong, Y.; Tong, Q.; Shan, W.; Xing, Z.; Wang, Y.; Wen, S.; Lou, Z. Arsenic transformation and adsorption by iron hydroxide/manganese dioxide doped straw activated carbon. *Appl. Surf. Sci.* **2017**, *416*, 618–627. [CrossRef]
10. Li, Y.; Cui, W.; Liu, L.; Zong, R.; Yao, W.; Liang, Y.; Zhu, Y. Removal of Cr(VI) by 3D TiO₂-graphene hydrogel via adsorption enriched with photocatalytic reduction. *Appl. Catal. B Environ.* **2016**, *199*, 412–423. [CrossRef]

11. Saleh, T.; Sari, A.; Tuzen, M. Effective adsorption of antimony(III) from aqueous solutions by polyamide-graphene composite as a novel adsorbent. *Chem. Eng. J.* **2017**, *307*, 230–238. [[CrossRef](#)]
12. Saleh, T.A. Simultaneous adsorptive desulfurization of diesel fuel over bimetallic nanoparticles loaded on activated carbon. *J. Clean. Prod.* **2018**, *172*, 2123–2132. [[CrossRef](#)]
13. Kumar, R.; Oves, M.; Almeelbi, T.; Al-Makishah, N.H.; Barakat, M. Hybrid chitosan/polyaniline-polypyrrole biomaterial for enhanced adsorption and antimicrobial activity. *J. Colloid Interface Sci.* **2017**, *490*, 488–496. [[CrossRef](#)] [[PubMed](#)]
14. Chotsuwan, C.; Asawapirom, U.; Shimoi, Y.; Akiyama, H.; Ngamaroonchote, A.; Jiemsakul, T.; Jirimitmongkon, K. Investigation of the electrochromic properties of tri-block polyaniline-polythiophene-polyaniline under visible light. *Synth. Met.* **2017**, *226*, 80–88. [[CrossRef](#)]
15. Wang, L.; Chen, Z.; Wen, H.; Cai, Z.; He, C.; Wang, Z.; Yan, W. Microwave assisted modification of activated carbons by organic acid ammoniums activation for enhanced adsorption of acid red 18. *Powder Technol.* **2018**, *323*, 230–237. [[CrossRef](#)]
16. Zhu, K.; Duan, Y.; Wang, F.; Gao, P.; Jia, H.; Ma, C.; Wang, C. Silane-modified halloysite/Fe₃O₄ nanocomposites: Simultaneous removal of Cr(VI) and Sb(V) and positive effects of Cr(VI) on Sb(V) adsorption. *Chem. Eng. J.* **2017**, *311*, 236–246. [[CrossRef](#)]
17. Chen, J.; Feng, J.; Yan, W. Influence of metal oxides on the adsorption characteristics of PPy/metal oxides for methylene blue. *J. Colloid Interface Sci.* **2016**, *475*, 26–35. [[CrossRef](#)]
18. Chang, C.-J.; Chao, P.-Y. Efficient photocatalytic hydrogen production by doped ZnS grown on Ni foam as porous immobilized photocatalysts. *Int. J. Hydrogen Energy* **2018**, *44*, 20805–20814. [[CrossRef](#)]
19. Zangeneh, H.; Zinatizadeh, A.; Habibi, M.; Akia, M.; Isa, M.H. Photocatalytic oxidation of organic dyes and pollutants in wastewater using different modified titanium dioxides: A comparative review. *J. Ind. Eng. Chem.* **2014**, *26*, 1–36. [[CrossRef](#)]
20. Paz, Y. Application of TiO₂ photocatalysis for air treatment: Patents' overview. *Appl. Catal. B* **2010**, *99*, 448–460. [[CrossRef](#)]
21. Li, Y.; Wang, W.; Qiu, X.; Song, L.; Meyer, H.M., III; Paranthaman, M.P.; Eres, G.; Zhang, Z.; Gu, B. Comparing Cr, and N only doping with (Cr, N)-codoping for enhancing visible light reactivity of TiO₂. *Appl. Catal. B* **2011**, *110*, 148–153. [[CrossRef](#)]
22. Wang, H.; Zhang, L.; Chen, Z.; Hu, J.; Li, S.; Wang, Z.; Liu, J.; Wang, X. Semiconductor heterojunction photocatalysts: Design, construction, and photocatalytic performances. *Chem. Soc. Rev.* **2014**, *43*, 5234–5244. [[CrossRef](#)] [[PubMed](#)]
23. Hsu, M.-H.; Chang, C.-J. S-doped ZnO nanorods on stainless-steel wire mesh as immobilized hierarchical photocatalysts for photocatalytic H₂ production. *Int. J. Hydrogen Energy* **2014**, *39*, 16524–16533. [[CrossRef](#)]
24. Chang, C.-J.; Wei, Y.-H.; Huang, K.-P. Photocatalytic hydrogen production by flower-like graphene supported ZnS composite photocatalysts. *Int. J. Hydrogen Energy* **2017**, *42*, 23578–23586. [[CrossRef](#)]
25. Ponzio, E.A.; Benedetti, T.M.; Torresi, R.M. Electrochemical and morphological stabilization of V₂O₅ nanofibers by the addition of polyaniline. *Electrochim. Acta* **2007**, *52*, 4419–4427. [[CrossRef](#)]
26. Malta, M.; Torresi, R.M. Electrochemical and kinetic studies of lithium intercalation in composite nanofibers of vanadium oxide/polyaniline. *Electrochim. Acta* **2005**, *50*, 5009–5014. [[CrossRef](#)]
27. Karim, M.R.; Yeum, J.H.; Lee, M.S.; Lim, K.T. Preparation of conducting polyaniline/TiO₂ composite submicron-rods by the gamma-radiolysis oxidative polymerization method. *React. Funct. Polym.* **2008**, *68*, 1371–1376. [[CrossRef](#)]
28. Zielińska, A.; Carreiró, F.; Oliveira, A.M.; Neves, A.; Pires, B.; Venkatesh, D.N.; Durazzo, A.; Lucarini, M.; Eder, P.; Silva, A.M.; et al. Polymeric Nanoparticles: Production, Characterization, Toxicology and Ecotoxicology. *Molecules* **2020**, *25*, 3731. [[CrossRef](#)]
29. Zhu, S.; Xu, T.; Fu, H.; Zhao, J.; Zhu, Y. Synergetic Effect of Bi₂WO₆ Photocatalyst with C₆₀ and Enhanced Photoactivity Under Visible Irradiation. *Environ. Sci. Technol.* **2007**, *41*, 6234–6239. [[CrossRef](#)]
30. Lee, S.L.; Chang, C.-J. Recent Developments about Conductive Polymer Based Composite Photocatalysts. *Polymers* **2019**, *11*, 206. [[CrossRef](#)]
31. Ma, J.; Dai, J.; Duan, Y.; Zhang, J.; Qiang, L.; Xue, J. Fabrication of PANI-TiO₂/rGO hybrid composites for enhanced photocatalysis of pollutant removal and hydrogen production. *Renew. Energy* **2020**, *156*, 1008–1018. [[CrossRef](#)]
32. Wang, N.; Chen, J.; Wang, J.; Feng, J.; Yan, W. Removal of methylene blue by Polyaniline/TiO₂ hydrate: Adsorption kinetic, isotherm and mechanism studies. *Powder Technol.* **2019**, *347*, 93–102. [[CrossRef](#)]
33. Shang, M.; Wang, W.; Sun, S.; Ren, J.; Zhou, L.; Zhang, L. Efficient Visible Light-Induced Photocatalytic Degradation of Contaminant by Spindle-Like PANI/BiVO₄. *J. Phys. Chem. C* **2009**, *113*, 20228–20233. [[CrossRef](#)]
34. Liu, X.-X.; Zhang, L.; Li, Y.-B.; Bian, L.-J.; Huo, Y.-Q.; Su, Z. Electrosynthesis of Polyaniline/SiO₂ Composite at high pH in the Absence of Extra Supporting Electrolyte. *Polym. Bull.* **2006**, *57*, 825–832. [[CrossRef](#)]
35. Manjunath, S.; Koppalkar, A.K.; Prasad, M.V.N.A. Dielectric Spectroscopy of Polyaniline/Stannic Oxide (PANI/SnO₂) Composites. *Ferroelectrics* **2008**, *366*, 22–28. [[CrossRef](#)]
36. Singh, N.; Kulkarni, M.V.; Lonkar, S.P.; Viswanath, A.K.; Khanna, P.K. CdS/Polyaniline Nanocomposites: Synthesis and Characterization. *Synth. React. Inorganic, Met. Nano-Metal Chem.* **2007**, *37*, 153–159. [[CrossRef](#)]
37. Li, G.; Zhang, C.; Peng, H.; Chen, K. One-Dimensional V₂O₅@Polyaniline Core/Shell Nanobelts Synthesized by an In Situ Polymerization Method. *Macromol. Rapid Commun.* **2009**, *30*, 1841–1845. [[CrossRef](#)]
38. Zhao, M.; Wu, X.; Cai, C. Polyaniline Nanofibers: Synthesis, Characterization, and Application to Direct Electron Transfer of Glucose Oxidase. *J. Phys. Chem. C* **2009**, *113*, 4987–4996. [[CrossRef](#)]
39. Khairy, M.; Kamar, E.M.; Yehia, M.; Masoud, E.M. High Removal Efficiency of Methyl Orange Dye by Pure and (Cu, N) Doped TiO₂/Polyaniline Nanocomposites. *Biointerface Res. Appl. Chem.* **2021**, *12*, 893–909. [[CrossRef](#)]

40. Qutub, N.; Singh, P.; Sabir, S.; Sagadevan, S.; Oh, W.C. Enhanced photocatalytic degradation of Acid Blue dye using CdS/TiO₂ nanocomposite. *Sci. Rep.* **2022**, *12*, 5759. [[CrossRef](#)]
41. Borah, J.P.; Barman, J.; Sarma, K.C. Structural and Optical Properties of ZnS Nanoparticles. *Chalcogenide Lett.* **2008**, *5*, 201–208.
42. Peng, X.; Schlamp, M.C.; Kadavanich, A.V.; Alivisatos, A.P. Epitaxial Growth of Highly Luminescent CdSe/CdS Core/Shell Nanocrystals with Photostability and Electronic Accessibility. *J. Am. Chem. Soc.* **1997**, *119*, 7019–7029. [[CrossRef](#)]
43. Mirov, S.B.; Fedorov, V.; Graham, K.; Moskalev, I.S.; Badikov, V.V.; Panyutin, V. Erbium fiber laser-pumped continuous-wave microchip Cr²⁺:ZnS and Cr²⁺:ZnSe lasers. *Opt. Lett.* **2002**, *27*, 909–911. [[CrossRef](#)] [[PubMed](#)]
44. Behboudnia, M.; Habibi-Yangjeh, A.; Jafari-Tarzanag, Y.; Khodayari, A. Facile and Room Temperature Preparation and Characterization of PbS Nanoparticles in Aqueous [EMIM][EtSO₄] Ionic Liquid Using Ultrasonic Irradiation. *Bull. Korean Chem. Soc.* **2008**, *29*, 53–56.
45. Kim, E.; Kim, D.; Ahn, B. Synthesis of Mesoporous TiO₂ and Its Application to Photocatalytic Activation of Methylene Blue and *E. coli*. *Bull. Korean Chem. Soc.* **2009**, *30*, 193–196. [[CrossRef](#)]
46. Huang, X.; Wang, G.; Yang, M.; Guo, W.; Gao, H. Synthesis of polyaniline-modified Fe₃O₄/SiO₂/TiO₂ composite microspheres and their photocatalytic application. *Mater. Lett.* **2011**, *65*, 2887–2890. [[CrossRef](#)]
47. Wang, N.; Li, J.; Lv, W.; Feng, J.; Yan, W. Synthesis of polyaniline/TiO₂ composite with excellent adsorption performance on acid red G. *RSC Adv.* **2015**, *5*, 21132–21141. [[CrossRef](#)]
48. Qutub, N.; Pirzada, B.M.; Umar, K.; Sabir, S. Synthesis of CdS nanoparticles using different sulfide ion precursors: Formation mechanism and photocatalytic degradation of Acid Blue-29. *J. Environ. Chem. Eng.* **2016**, *4*, 808–817. [[CrossRef](#)]
49. Lu, X.; Yu, Y.; Chen, L.; Mao, H.; Zhang, W.; Wei, Y. Preparation and characterization of polyaniline microwires containing CdS nanoparticles. *Chem. Commun.* **2004**, *13*, 1522–1523. [[CrossRef](#)]
50. Li, Q.; Zhang, C.; Li, J. Photocatalysis and wave-absorbing properties of polyaniline/TiO₂ microbelts composite by in situ polymerization method. *Appl. Surf. Sci.* **2010**, *257*, 944–948. [[CrossRef](#)]
51. Savitha, K.; Prabu, H.G. One-pot synthesis of PANI–TiO₂ (anatase) hybrid of low electrical resistance using TiCl₄ as precursor. *Mater. Chem. Phys.* **2011**, *130*, 275–279. [[CrossRef](#)]
52. Nyamukamba, P.; Moloto, M.J.; Mungondori, H. Visible Light-Active CdS/TiO₂ Hybrid Nanoparticles Immobilized on Polyacrylonitrile Membranes for the Photodegradation of Dyes in Water. *J. Nanotechnol.* **2019**, *2019*, 5135618. [[CrossRef](#)]
53. Qutub, N.; Pirzada, B.M.; Umar, K.; Mehraj, O.; Muneer, M.; Sabir, S. Synthesis, characterization and visible-light driven photocatalysis by differently structured CdS/ZnS sandwich and core-shell nanocomposites. *Phys. E Low-Dimens. Syst. Nanostructures* **2015**, *74*, 74–86. [[CrossRef](#)]
54. He, K.; Li, M.; Guo, L. Preparation and photocatalytic activity of PANI-CdS composites for hydrogen evolution. *Int. J. Hydrogen Energy* **2012**, *37*, 755–759. [[CrossRef](#)]
55. Nur, H.; Misnon, I.I.; Wei, L.K. Stannic Oxide-Titanium Dioxide Coupled Semiconductor Photocatalyst Loaded with Polyaniline for Enhanced Photocatalytic Oxidation of 1-Octene. *Int. J. Photoenergy* **2007**, *2007*, 098548. [[CrossRef](#)]
56. Du, X.-S.; Zhou, C.-F.; Mai, Y.-W. Facile Synthesis of Hierarchical Polyaniline Nanostructures with Dendritic Nanofibers as Scaffolds. *J. Phys. Chem. C* **2008**, *112*, 19836–19840. [[CrossRef](#)]
57. Mallick, K.; Witcomb, M.J.; Scurrall, M.; Strydom, A. In-situ chemical synthesis route for a fiber shaped gold-polyaniline nanocomposite. *Gold Bull.* **2008**, *41*, 246–250. [[CrossRef](#)]
58. Dutta, K.; De, S. Optical and electrical characterizations of self-assembled CdS nanorods—Polyaniline composites. *J. Appl. Phys.* **2007**, *101*, 093711. [[CrossRef](#)]
59. Ramakrishnan, R.; Sudha, J.D.; Reena, V.L. Nanostructured Polyaniline-Polytitanate-Clay Composite for Photocatalytic Applications: Preparation and Properties. *RSC Adv.* **2012**, *2*, 6228–6236. [[CrossRef](#)]
60. Gu, L.; Wang, J.; Qi, R.; Wang, X.; Xu, P.; Han, X. A novel incorporating style of polyaniline/TiO₂ composites as effective visible photocatalysts. *J. Mol. Catal. A Chem.* **2012**, *357*, 19–25. [[CrossRef](#)]
61. Lu, X.; Gao, H.; Chen, J.; Chao, D.; Zhang, W.; Wei, Y. Poly(acrylic acid)-guided synthesis of helical polyaniline/CdS composite microwires. *Nanotechnology* **2005**, *16*, 113–117. [[CrossRef](#)]
62. Khiew, P.; Huang, N.M.; Radiman, S.; Ahmad, S. Synthesis and characterization of conducting polyaniline-coated cadmium sulphide nanocomposites in reverse microemulsion. *Mater. Lett.* **2004**, *58*, 516–521. [[CrossRef](#)]
63. Ummartyotin, S.; Bunnak, N.; Juntaro, J.; Sain, M.; Manuspiya, H. Synthesis and Luminescence Properties of ZnS and Metal (Mn, Cu)-doped-ZnS Ceramic Powder. *Solid State Sci.* **2012**, *14*, 299–304. [[CrossRef](#)]
64. Devi, B.S.R.; Raveendran, R.; Vaidyan, A.V. Synthesis and characterization of Mn²⁺-doped ZnS nanoparticles. *Pramana* **2007**, *68*, 679–687. [[CrossRef](#)]
65. Niziol, J.; Sniechowski, M.; Podraza-Guba, A.; Pielichowski, J. Alternative Oxidizers in Polyaniline Synthesis. *Polym. Bull.* **2011**, *66*, 761–770. [[CrossRef](#)]
66. Girginer, B.; Galli, G.; Chiellini, E.; Bicak, N. Preparation of stable CdS nanoparticles in aqueous medium and their hydrogen generation efficiencies in photolysis of water. *Int. J. Hydrogen Energy* **2008**, *34*, 1176–1184. [[CrossRef](#)]
67. Uwe, H.; Neil, G. The Scherrer Equation Versus the ‘Debye-Scherrer Equation’. *Nat. Nanotechnol.* **2011**, *6*, 534.
68. Scherrer, P. Determination of the Size and Internal Structure of Colloidal Particles using X-rays. *Göttinger Nachr. Math. Phys.* **1918**, *2*, 98–100.

69. Chen, X.; Xu, H.; Xu, N.; Zhao, F.; Lin, W.; Lin, G.; Fu, Y.; Huang, Z.; Wang, H.; Wu, M. Kinetically Controlled Synthesis of Wurtzite ZnS Nanorods through Mild Thermolysis of a Covalent Organic–Inorganic Network. *Inorg. Chem.* **2003**, *42*, 3100–3106. [[CrossRef](#)]
70. Li, Q.; Wang, C. Fabrication of wurtzite ZnS nanobelts via simple thermal evaporation. *Appl. Phys. Lett.* **2003**, *83*, 359–361. [[CrossRef](#)]
71. Oh, M.; Kim, S. Synthesis and electrochemical analysis of polyaniline/TiO₂ composites prepared with various molar ratios between aniline monomer and para-toluenesulfonic acid. *Electrochimica Acta* **2012**, *78*, 279–285. [[CrossRef](#)]
72. Tarver, J.; Yoo, J.E.; Dennes, T.J.; Schwartz, J.; Loo, Y.-L. Polymer Acid Doped Polyaniline Is Electrochemically Stable beyond pH 9. *Chem. Mater.* **2008**, *21*, 280–286. [[CrossRef](#)]
73. Fan, J.; Ji, X.; Zhang, W.; Yan, Y. Preparation and Photoelectronic Properties of Q-CdS/Polyaniline (PANI) Nanocomposites. *CJI* **2004**, *6*, 45–50.
74. Singh, V.; Sharma, P.; Chauhan, P. Synthesis of CdS nanoparticles with enhanced optical properties. *Mater. Charact.* **2011**, *62*, 43–52. [[CrossRef](#)]
75. Heera, T.; Cindrella, L. PbS/CoS–Pani Composite Semiconductor Films. *Mater. Sci. Semicond. Processing* **2011**, *14*, 151–156. [[CrossRef](#)]
76. Rathore, K.S.; Patidar, D.; Janu, Y.; Saxena, N.S.; Sharma, K.; Sharma, T.P. Structural and Optical Characterization of Chemically Synthesized ZnS Nanoparticles. *Chalcogenide Lett.* **2008**, *5*, 105–110.
77. Zhang, S.; Chen, Q.; Jing, D.; Wang, Y.; Guo, L. Visible photoactivity and antiphotocorrosion performance of PdS–CdS photocatalysts modified by polyaniline. *Int. J. Hydrogen Energy* **2012**, *37*, 791–796. [[CrossRef](#)]
78. Zhang, H.; Zhu, Y. Significant Visible Photoactivity and Antiphotocorrosion Performance of CdS Photocatalysts after Monolayer Polyaniline Hybridization. *J. Phys. Chem. C* **2010**, *114*, 5822–5826. [[CrossRef](#)]
79. Deshpande, A.; Shah, P.; Gholap, R.; Gupta, N.M. Interfacial and physico-chemical properties of polymer-supported CdS–ZnS nanocomposites and their role in the visible-light mediated photocatalytic splitting of water. *J. Colloid Interface Sci.* **2009**, *333*, 263–268. [[CrossRef](#)]
80. Wu, L.; Yu, J.; Fu, X. Characterization and photocatalytic mechanism of nanosized CdS coupled TiO₂ nanocrystals under visible light irradiation. *J. Mol. Catal. A Chem.* **2006**, *244*, 25–32. [[CrossRef](#)]
81. Nasuha, N.; Hameed, B.H.; Okoye, P.U. Dark-Fenton oxidative degradation of methylene blue and acid blue 29 dyes using sulfuric acid-activated slag of the steel-making process. *J. Environ. Chem. Eng.* **2021**, *9*, 10483. [[CrossRef](#)]
82. Nasuha, N.; Ismail, S.; Hameed, B.H. Activated electric arc furnace slag as an effective and reusable Fenton-like catalyst for the photodegradation of methylene blue and acid blue 29. *J. Environ. Manag.* **2017**, *196*, 323–329. [[CrossRef](#)] [[PubMed](#)]
83. Khanday, W.A.; Asif, M.; Hameed, B. Cross-linked beads of activated oil palm ash zeolite/chitosan composite as a bio-adsorbent for the removal of methylene blue and acid blue 29 dyes. *Int. J. Biol. Macromol.* **2017**, *95*, 895–902. [[CrossRef](#)] [[PubMed](#)]
84. Sahoo, M.K.; Sayoo, L. Removal of Acid Blue 29 in aqueous solution by Fenton and Fenton-like processes. *Desalination Water Treat.* **2014**, *52*, 3411–3420. [[CrossRef](#)]
85. Salem, I.A.; El-Ghamry, H.A.; El-Ghobashy, M.A. Catalytic decolorization of Acid blue 29 dye by H₂O₂ and a heterogeneous catalyst. *Beni-Suef Univ. J. Basic Appl. Sci.* **2014**, *3*, 186–192. [[CrossRef](#)]
86. Chen, C.; Chaudhary, A.; Grimes, S. The effect of sodium hydroxide in photolytic and photocatalytic degradation of Acid Blue 29 and Ethyl Violet. *Dye. Pigment.* **2007**, *73*, 55–58. [[CrossRef](#)]